Proceedings of the ASME 2015 Conference on Smart Materials, Adaptive Structures and Intelligent Systems
SMASIS2015
September 21-23, 2015, Colorado Springs, Colorado, USA

SMASIS2015-8975

COMPUTATIONALLY EFFICIENT ANALYSIS OF SMA SENSORY PARTICLES EMBEDDED IN COMPLEX AEROSTRUCTURES USING A SUBSTRUCTURE APPROACH

Brent Bielefeldt
Department of Aerospace Engineering
Texas A&M University
College Station, Texas 77843

Jacob Hochhalter
NASA Langley Research Center
Hampton, Virginia 23681

Darren Hartl
Department of Aerospace Engineering
Texas A&M University
College Station, Texas 77843
Email: darren.hartl@tamu.edu

ABSTRACT

The Digital Twin concept represents an innovative method to monitor and predict the performance of an aircraft's various subsystems. By creating ultra-realistic multi-physical computational models associated with each unique aircraft and combining them with known flight histories, operators could benefit from a real-time understanding of the vehicle's current capabilities. One important facet of the Digital Twin program is the detection and monitoring of structural damage. Recently, a method to detect fatigue cracks using the transformation response of shape memory alloy (SMA) particles embedded in the aircraft structure has been proposed. By detecting changes in the mechanical and/or electromagnetic responses of embedded particles, operators could detect the onset of fatigue cracks in the vicinity of these particles. In this work, the development of a finite element model of an aircraft wing containing embedded SMA particles in key regions will be discussed. In particular, this model will feature a technique known as substructure analysis, which retains degrees of freedom at specified points key to scale transitions, greatly reducing computational cost. By using this technique to model an aircraft wing subjected to loading experienced during flight, we can simulate the response of these localized particles while also reducing computation time. This new model serves to demonstrate key aspects of this detection technique. Future work, including the determination of the material properties associated with these particles as well as exploring the positioning of these particles for optimal crack detection, is also discussed.

1 INTRODUCTION

The ability to monitor and predict the real-time performance of an aircraft is of growing importance to the aerospace industry. As their capabilities continue to grow, future aircraft and spacecraft will undergo more strenuous missions for longer periods of time, which may surpass the conditions that can be applied during ground testing. Additionally, future craft will feature more complex materials which, while improving aircraft performance, exhibit behavior that is more difficult to predict. To address this growing need, the Digital Twin concept was proposed for future NASA and Air Force vehicles. A Digital Twin is an ultra-realistic multi-physical computational aircraft model that simulates the capabilities of various subsystems to create a near real-time understanding of the aircraft [1]. Each vehicle would have its own unique Digital Twin that would record its operational history as well as any maintenance or changes made to the vehicle. Pairing this history with flight simulations would allow operators to estimate the current performance of the craft as well as modify missions to maximize vehicle lifetime [2]. The Digital Twin program would also allow for the ability to simulate future missions prior to launch, enabling operators to adjust missions based on current vehicle performance and predictions of mission success.

One important aspect of the Digital Twin concept is the monitoring of structural health of an aircraft, particularly damage stemming from the formation of fatigue cracks. Such information would be used to update the multi-physical Digital Twin models. Current detection techniques rely on *time-based maintenance* involving disassembling the aircraft, part-by-part inspection, and repair if necessary [3]. While this has proven to be effective in reducing the number of incidents involving aircraft structural failure, it is an expensive process that can lead to other complications, such as incidental damage of structural components or improper reassembly. Furthermore, these routine inspections are based on experiences with similar aircraft operating in similar conditions [1]. Since each aircraft is unique, vehicles in minimal danger of structural failure could undergo inspection, wasting both time and man-power. A detection method unique to each aircraft, such as one combined with its Digital Twin, would be more efficient.

Recently, a non-destructive evaluation (NDE) method has been proposed that would allow for the real-time detection and monitoring of fatigue cracks in an aircraft structure [4]. By embedding stress-sensitive active material particles into aircraft components, the formation of fatigue cracks can be identified by detecting changes in the mechanical responses of particles in the vicinity of structural damage. This *condition-based maintenance* could lead to the earlier detection of fatigue cracks while also reducing the need for traditional inspection methods [3]. Additionally, this method could be utilized by an aircraft's Digital Twin to monitor the progression of fatigue cracks as well as predict the formation of fatigue cracks during flight. If a fatigue crack is detected and its position and size is transferred to the Digital Twin, simulations could predict whether current flight conditions or mission objectives would jeopardize the structural integrity of the aircraft [2]. This method also has the benefit of being unique to each aircraft; rather than base inspections on the maintenance history of similar aircraft operating in similar conditions, each aircraft could be monitored and repaired on an as-needed basis.

The detection of this structural damage is based upon the unique material response of active materials, namely shape memory alloys (SMAs), when subjected to specific conditions [5, 6]. SMAs exhibit unique mechanical responses due to temperature- or stress-induced phase transformations [7]. In the case of this NDE method, as a fatigue crack begins to propagate the local stress field in the aircraft component will evolve in strength and direction; at a certain stress-level, a particle in the vicinity of the damage zone will transform from the *austenite* phase to the *martensite* phase, which exhibits altered material properties that can be detected using a number of different methods depending on the material. Figure 1 depicts this phenomenon. One method involves the acoustic sensing of phase transformation in certain SMAs such as NiTi. Oishi and Nagai demonstrated such a method using SMA wires; using acoustic signals produced during phase transformation, they detected changes in strain up to 5% [8]. Another method involves the magnetic sensing of martensite generation or variant reorientation in magnetic SMA (MSMA) particles under a sufficient local mechanical load [9].

To visualize this method, an aircraft wing with a single-trial SMA particle embedded in a rib near a stress concentration was modeled using a finite element approach. However, since an aircraft wing is a complex structure spanning dozens of meters and containing multiple parts, an associated finite element model must consider hundreds of thousands of elements and full analysis of a wingbox and rib containing an SMA particle would be very computationally expensive. To address this issue, the model (Figure 2) was constructed using a method known as *substructuring*, which retains degrees of freedom only at specified points. This method will allow for future detailed studies of sensory particle placement relative to stress concentrations for a wide range of aerostructure loads. This paper further discusses this modeling method as well as the response of the SMA particle when subjected to stress concentrations during loading.

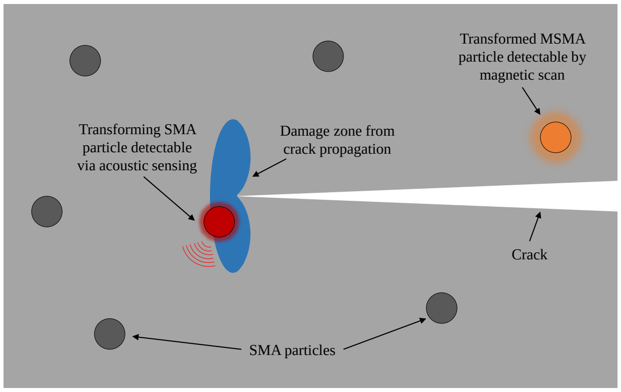

FIGURE 1: Diagram of a NDE method for detecting and monitoring fatigue damage using active materials.

2 MODELING TECHNIQUES

2.1 Substructure Modeling

A substructure is a collection of elements from which the internal degrees of freedom (DOFs) have been eliminated; only nodes/DOFs specified during the generation of the substructure are retained and recognized externally at the usage level [10]. Specifically, the stiffnesses between all retained nodes is precomputed and made available for later coupling to other domains, including other substructures. Solid modeling using substructures has many computational advantages. As a result of keeping only specified degrees of freedom, the stiffness matrix associated with the model is relatively small compared to the general stiffness matrix that includes DOFs at every node. Additionally, stiffness calculations are done on a substructure only once; this can improve efficiency when analyzing an unchanged part in multiple models or when the same part appears in a model multiple times. Substructure modeling also allows for large and complex models to be built as layered substructures, stacked level by level until the whole structure is complete. However, there are several restrictions on the use of substructures, namely that the model re-

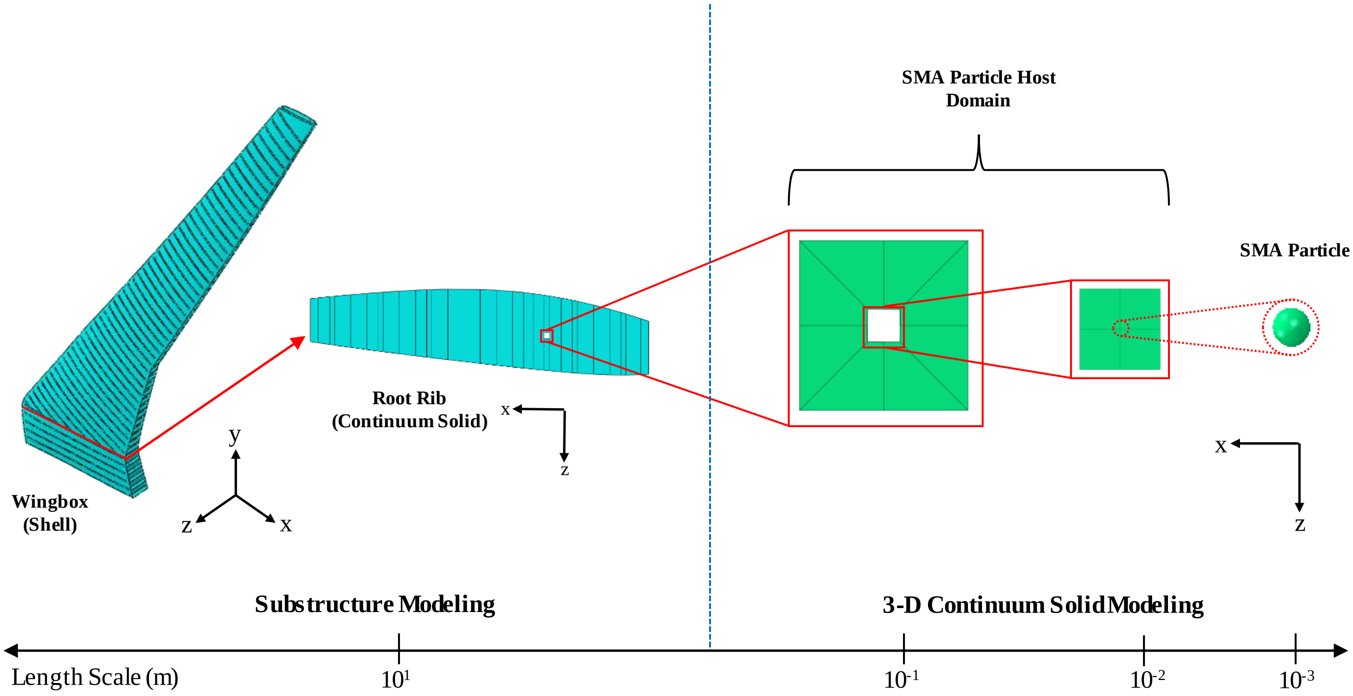

FIGURE 2: Assembly of the wingbox using a combination of substructure and solid modeling.

sponse must be linear. This prevents the use of substructure modeling on parts containing SMA material. (There are substructure models that incorporate non-linearity, such as one developed by Wu and Haug [11], but this is beyond the current scope of this study.) There are also limitations to the number of DOFs you can retain in each analysis. Nonetheless, substructures have become a viable method for the modeling of complex structures. Substructure modeling has been implemented by Dougherty et al. in the modeling of plasticity-induced crack closure in modified 1070 steel [12], as well the modeling of fatigue crack growth in marine structures [13, 14].

Generally, substructures are used to model multiple small parts in a larger overall model. However, as mentioned above, they are not compatible with the nonlinear behavior of an SMA particle, which is the smallest body considered herein. Therefore, in this analysis a different approach was used. Substructure modeling is used to transition from a large scale (full wingbox) to a small scale (SMA particle with a diameter of 1.27 mm). The wingbox and most of the root rib are modeled using substructures, while a small section of the root rib was modeled using 3-D continuum solids. This will be discussed in more detail in the next section.

2.2 Computational Model

2.2.1 Shell-Based Substructure A working model of an aircraft wing was constructed in Abaqus using finite element files developed by the Common Research Model (CRM), a NASA program that established experimental databases to aid researchers in validating specific components of computational fluid dynamic programs [15–17]. The wing is based on a transonic commercial transport configuration designed to fly at a cruise Mach number of M=0.85 with an aspect-ratio of AR=9.0, a taper-ratio of λ=0.275, a span of 58.76 m (2,313 in), and a gross vehicle weight of approximately 226,800 kg (500,000 $\mathrm{lb_m}$). These parameters are similar to that of a Boeing 787-8. The structure is made of an isotropic aluminum with an elastic modulus of E=70,000 MPa (10,000 ksi), Poisson's raito of ν=0.32, and a mass density of ρ=2768 $\mathrm{kg/m^3}$ (0.1 $\mathrm{lb_m/in^3}$) [18]. For the purposes of this study, the wing is assumed to experience an elliptical loading distribution with forces applied to the main spar of the wing. A local coordinate system is defined with its origin located at the intersection of the root rib and main spar and its x-axis along the main spar (denoted x') (Figure 3). We approximate this load condition by applying a concentrated force f_i to

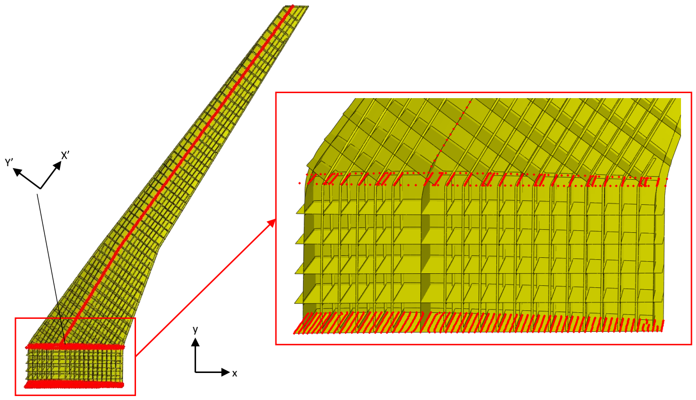

FIGURE 3: Retained DOFs on the wingbox substructure. DOFs along the span are retained for applying loading, while DOFs pictured in the box are retained for root rib attachment (middle) and application of boundary conditions (bottom). A local coordinate system is defined with its origin located at the intersection of the root rib and main spar.

each node at position x'_i with magnitude

$$f_i(x'_i) = \int_{x'_i}^{x'_{i+1}} \frac{2W}{\pi L}\sqrt{1-(\frac{x'}{L})^2}\,dx' \tag{2.1}$$

where W is the weight of the aircraft[1], L is the length of the span, and x' is the distance along the span from each node to the root rib. It can be shown from this equation that a single wing is subjected to a load of $W/2$.

The provided CRM wingbox finite element model contains a pre-meshed shell-based geometry consisting of 57,292 linear shell elements with reduced integration[2], corresponding to 52,393 nodes and 314,358 total DOFs. The large number of DOFs make the model an ideal candidate for substructure modeling. As stated in Section 2.1, substructure modeling is being used to transition across length scales (i.e. the transition from the entire wingbox to a single rib); therefore the root rib was removed from the wingbox model prior to substructure generation. Nodes are retained in the following locations:

1. along the negative y-surface of the wingbox (for application of boundary conditions)
2. at points where the root rib intersects spars/longerons (for the attachment of the root rib to the substructure)
3. along the positive z-edge of the main spar (for the application of loads)

This method results in 6,366 retained DOFs (Figure 3), or a reduction of nearly 98% from a non-substructure wingbox model with the root rib removed.

2.2.2 Solid-Based Substructure

After the removal of the root rib from the wingbox, a rib of the same dimensions and material was modeled. The rib spans approximately 7.366 m (290 in) and is partitioned along axes where the rib is intersected by spars and longerons. A small square measuring 130 x 130 mm (5.14 x 5.14 in) was removed from an area free from such intersections; this is the area where the SMA particle is embedded. It is important to note that, unlike the shell-based original model, this rib is constructed as a solid part with a thickness of 6 mm (0.24 in) (matching the shell thickness of the original rib). This use of a solid rib is required to ensure proper tied interface with the domain containing the embedded SMA particle, which is also a solid model. The rib contains 1,508 linear elements with reduced integration[3], or 19,104 DOFs. During the meshing of this part, attempts were made to keep the mesh as close to the CRM as possible, leading to a coarse mesh. To further reduce computation as well as display the ability of substructure modeling to bridge multiple length scales, the root rib is also generated as a substructure. Nodes are retained

1. at points where the root rib must be "tied" to the wingbox substructure (along the top, bottom, and partitions where the rib is intersected by spars/longerons)
2. along edges where the SMA particle host domain will be connected to the rib substructure

This method results in 5,976 retained DOFs (Figure 4), or a reduction of around 69% from the solid rib model.

The root rib (Figure 4) is attached to the wingbox substructure (Figure 3) using the node-based "tie" constraint in Abaqus [10], which enforces the constraint that pairs of nodes from separate parts have identical translational and rotational motion. Analysis was run to ensure the change in element type between wingbox and rib did not result in inconsistent behavior during loading generated using Eqn. 2.1. Figure 5 shows that the behavior of the solid rib is relatively consistent with that of the shell-based rib and that the ties have been properly implemented.

To replicate an SMA particle's response to a stress concentration or structural damage, two geometric cases are considered. The first of these considers a hole of radius r=44.5 mm (1.75 in) located 109 mm (4.29 in) above the SMA particle host domain

---

[1] In this study, we reduce this weight to the maximum zero-fuel weight of a Boeing 787-8 (161,000 kg or 355,000 lb_m) (cf. [15]) and neglect the weight of the engine (approximately 5,600 kg or 13,000 lb_m) as well as the structural weight of the wing itself (approximately 11,500 kg or 25,200 lb_m). Thus, at 1 G the wing experiences a total lifting force of approximately 625,000 N (140,000 lb_m).

[2] Because of the size and number of elements of the model, linear elements were chosen over quadratic elements.

[3] Linear elements were used on the rib structure to maintain consistency of the model.

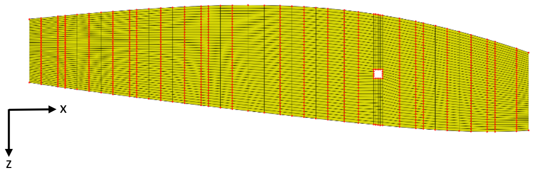

FIGURE 4: Retained DOFs on the rib substructure (shown by red dots). DOFs are retained where the rib is intersected by spars/longerons modeled in the wingbox substructure as well as where the SMA particle host domain is attached to the substructure.

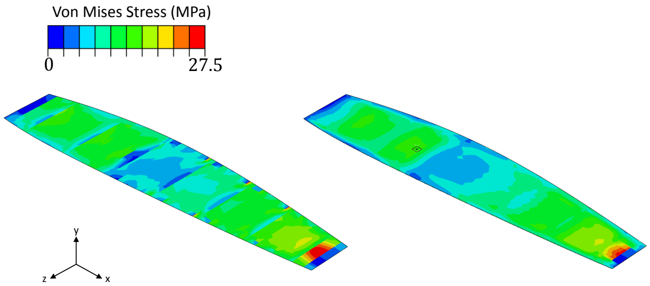

FIGURE 5: Comparison of local stress results using the original shell-based root rib (left) to those generated using a solid-based root rib (right) during 1 G loading. The solid rib captures the original response and also provides a better transition to the solid-element particle host domain.

(Figure 6b). This hole is introduced to provide a stress concentration in the vicinity of the particle. The second case introduces a crack of width=0.254 mm (0.01 in) and length=64.3 mm (2.53 in) running from the base of the hole towards the SMA particle host domain (Figure 6c). This crack introduces further stress concentrations and demonstrates a key aspect of this detection method.

2.2.3 SMA Constituative Model

A detailed description of the thermomechanical constituative model for SMAs used is this study can be found elsewhere [19]. However, a brief summary is provided here to generate an understanding of the underlying behavior of this material. The utilized model is three-dimensional and phenomenological. It centers on the generation and recovery of transformation strains that occur as result of martensitic reversible phase transformation. The model considers three external state variables (two tensorial and one scalar). These are the stress σ, the total infinitesimal strain ε, and the absolute temperature T. Two internal state variables are also considered: the inelastic (but recoverable) transformation strain ε^t and the total martensitic volume fraction ξ. The total strain is assumed to be additively decomposed into thermoelastic and inelastic terms, and is related to the stress and temperature via Hooke's Law:

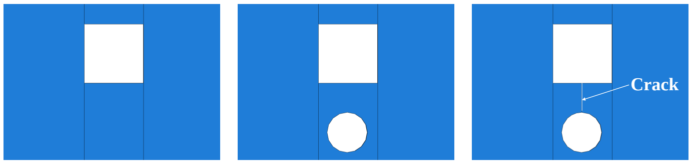

(a) (b) (c)

FIGURE 6: Local region of rib substructure with SMA particle region (square) removed with a) no damage or stress concentration, b) stress concentration in the form of a hole, and c) damage in the form of a crack propagating from the hole towards the SMA particle.

$$\varepsilon = \boldsymbol{S}(\xi)\sigma + \alpha(T - T_0) + \varepsilon^t \tag{2.2}$$

where $\boldsymbol{S}(\xi)$ is the linearly phase-dependent fourth-order compliance tensor, α is the second-order coefficient of thermal expansion tensor, and T_0 is a reference temperature. The compliance tensor $\boldsymbol{S}(\xi)$ is determined using a rule of mixtures between the compliance tensors of the austenitic and martensitic phases, $\boldsymbol{S}^A$ and $\boldsymbol{S}^M$, respectively:

$$\boldsymbol{S}(\xi) = \boldsymbol{S}^A + \xi(\boldsymbol{S}^M - \boldsymbol{S}^A) = \boldsymbol{S}^A + \xi\Delta\boldsymbol{S} \tag{2.3}$$

Constraints inspired by the methods of classical plasticity are placed on evolution of the martensitic volume fraction ξ, given by:

$$\Phi^t \leq 0, \qquad \dot{\xi}\Phi^t = 0, \qquad 0 \leq \xi \leq 1 \tag{2.4}$$

where Φ^t is the transformation function. These constraints bound the martensitc volume fraction between 0 (pure austenite) and 1 (pure martensite). To ensure positive dissipation during forward and reverse transformations, a branched form of Φ^t is proposed:

$$\Phi^t(\sigma, T, \xi) = \hat{\Phi}^t(\sigma) + p(\sigma, T, \xi) + \begin{cases} -Y; & \dot{\xi} \geq 0 \\ Y; & \dot{\xi} \leq 0 \end{cases} \tag{2.5}$$

where $\hat{\Phi}^t(\sigma)$ is the shape of the transformation in the space of the given stress components and $p(\sigma, T, \xi)$ describes both the transformation hardening and the dependence of the transformation stresses on temperature. It takes the form:

$$p(\sigma,T,\xi) = \frac{1}{2}\sigma \cdot \Delta\boldsymbol{S}\sigma + \rho\Delta s_0 T - \rho\Delta u_0 - f^t(\xi) \tag{2.6}$$

where $\rho\Delta s_0$ represents the entropy difference between austenite and martensite, $\rho\Delta u_0$ represents the internal energy difference between austenite and martensite, and f^t is the hardening function given by:

$$f^t(\xi) = \begin{cases} \frac{1}{2}a_1(1+\xi^{N_1} - (1-\xi)^{n_2} + a_3; & \dot{\xi} \geq 0 \\ \frac{1}{2}a_2(1+\xi^{N_3} - (1-\xi)^{n_4} + a_3; & \dot{\xi} \leq 0 \end{cases} \tag{2.7}$$

The smoothness of the transformation hardening function can be tuned by adjusting { n_1, n_2, n_3, n_4 } such that $0 < n_i \leq 1$, i=1,...,4. Assuming maximum transformation dissipation, the inelastic transformation strain evolves such that the time rate of change of its magnitude is proportional to the rate of change of the martensitic volume fraction while its direction is normal to the shape $\hat{\Phi}^t$ in the stress space:

$$\dot{\varepsilon}^t = \dot{\xi}\frac{\partial\hat{\Phi}^t(\sigma)}{\partial\sigma} \tag{2.8}$$

This model does not take into account plastic yielding of the SMA, but it is assumed that the particles will not reach such high stresses. Furthermore, if such high stresses occur the martensite will be retained and transformation associated changes (e.g. change in magnetization when considering MSMAs) will be made permanent [20]. Additionally, this model does not take into account the fatigue behavior of the SMA. Cyclical structural loading is not expected to cause transformation in the particles. Since a crack is expected to propagate past a given particle only once, a one-time transformation is considered.

2.2.4 Three-Dimensional Continuum Domains

To simulate an SMA particle embedded in the root rib, itself a component of the full wing, a smaller nested-structure was created, consisting of a 130 x 130 mm (5.14 x 5.14 in) square, a 25.4 x 25.4 mm (1.0 x 1.0 in) square, and a particle with radius r=1.27 mm (0.05 in). The nested squares consist of isotropic aluminum with the same material properties as the wingbox and root rib, while the properties of the isotropic SMA particle are given in Table 1. These properties are preliminary results from a material parameter study that will be published in future work. A nominal temperature of 298 K is applied to the entire structure.

TABLE 1: SMA Material Properties.

Property	Value
(Thermoelastic Properties)	
$E^M = E^A$	75,000 MPa
$\nu^M = \nu^A$	0.33
(Phase Diagram Properties)	
M_s, M_f	290 K, 260 K
A_s, A_f	313 K, 334 K
$C^M = C^A$	7 MPa/K
(Transformation Properties)	
H	3.0%
k_t	7.52x10^{-3}/MPa
$n_1 = n_3 = n_4$	0.9
n_2	0.3

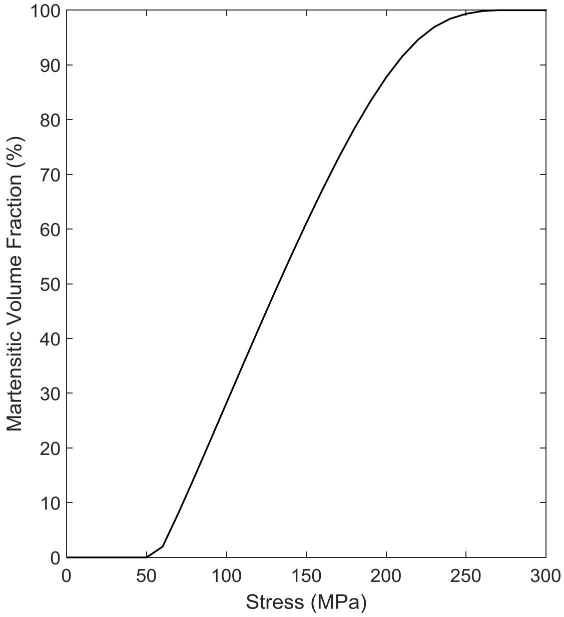

FIGURE 7: Martensitic volume fraction as a function of stress during forward transformation for the material parameters given in Table 1.

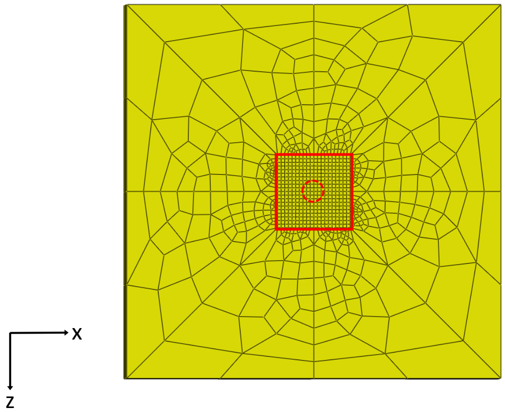

FIGURE 8: Assembly of SMA particle host domain using Abaqus tie constraints. Constraints (denoted by solid lines) are applied to the smaller domain and the particle (not shown).

Since tie constraints allow for the rapid transition of mesh densities, the smaller housing is tied to the larger housing, with the particle tied to an inner surface of the smaller housing (Figure 8). Each part consists of linear elements with reduced integration, with a combined total of 9,017 elements (or 43,446 DOFs). The nested structure is then tied to the rib substructure using additional tie constraints. Altogether, the entire substructure-based wingbox, root rib, SMA particle host domain, and SMA particle model consists of **roughly 15%** of the number of DOFs that would have been included had the model not been aided by substructure modeling.

3 RESULTS

The shell-based model of the wing was loaded using the method discussed in Section 2.2.1. Figure 9 depicts the wing loaded to 1 G in the positive z-direction, which is the loading typically experienced by the wing during cruise. The stress is distributed evenly along the span of the wing in the desired and efficient manner.Given the applied nominal temperature and assumed transformation properties of the SMA particle, analysis of the particle's behavior during unloading was deemed unnecessary. The temperature at which the particle will begin transformation back into the austenite phase is above the applied nominal temperature; therefore, the only change in the behavior of the particle would be a change in the elastic response, which is irrelevant for this damage detection method.

The model was assembled as discussed in Section 2.2. As analysis is run, loads are applied to the pre-computed wingbox substructure. The response of the wingbox is passed to the pre-computed root rib substructure via tie constraints, which in turn passes its response to the solid continuum particle host domain. The proper implementation of the tie constraint between the wingbox and root rib has already been shown (Figure 5). To ensure that the tie constraints between the root rib and particle host domain were implemented correctly, a trial test was first performed by considering a particle host domain *without a particle* with the same mesh density as the root rib (i.e. as if the rib was one continuous part). Figure 10 confirms that the constraints are behaving as expected. Any differences in the stress fields of the root rib and particle host domain in later analyses can then be attributed to mesh transitions.

The model was then subjected to loading between -2 G

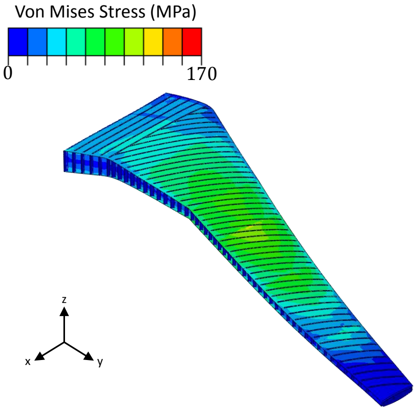

FIGURE 9: Shell-based wing loaded to 1 G via an assumed elliptical load distribution applied to the main spar.

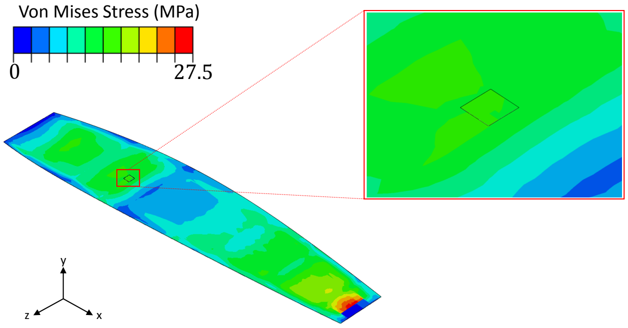

FIGURE 10: Root rib stress contour when the overall wing is loaded to 1 G. A solid "test" square of the same mesh density tied to the root rib. The lack of localized stress field effects associated with this tie region indicates that the constraint is behaving correctly.

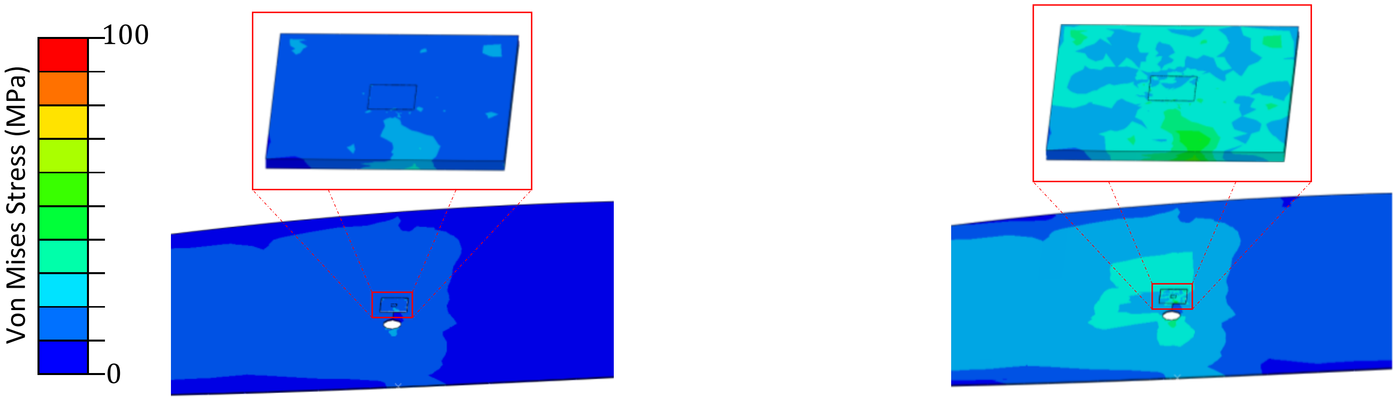

(a) 1 G

(b) 2 G

(c) 3,G

(d) 4 G

FIGURE 11: Local region of rib substructure with SMA particle region (square) removed with a) no damage or stress concentration, b) stress concentration in the form of a hole, and c) damage in the form of a crack propagating from the hole towards the SMA particle.

and 4 G. These loading conditions are taken from Federal Aviation Regulation commercial design practices, including simplified gust/turbulence loads (+3.75 G/-2.0 G) and basic maneuver loads (2.5 G) [21]. Figure 11 shows the response of the root rib with crack damage at various loads. The crack leads to further stress concentration within the particle host domain and therefore higher stresses felt by the particle, eventually leading to phase transformation.

The basis for this damage detection method centers around the response of an SMA particle to higher stress states. To quantify this response, the particle volume-averaged *martensitic volume fraction* (MVF), $\hat{\xi}$, was calculated. This is given by

$$\hat{\xi} = \frac{1}{V}\int \xi(\underline{x})dV \approx \frac{1}{V}\sum_{i=1}^{n} \xi_i V_i \tag{3.9}$$

where $\xi(\underline{x})$ is the local continuum MVF value, ξ_i and V_i are the MVF and volume at the i^{th} integration point, respectively, n is the number of integration points in the particle, and V is the total volume of the particle. Figure 12 shows the MVF for all three root rib configurations (cf. Figure 6) considered as a function of the load applied to the wing. The particle in embedded in the unmodified rib experiences almost no martensitic transformation for loads ranging from -2 G to 4 G. The stress concentration introduced by a hole in the root rib similarly causes almost no particle transformation until subjected to extremely high loads. However, the particle experiencing stress concentration caused by crack damage experiences a noticeable amount of martensitic transformation. It is also interesting to note that positive lifting loads induce a greater amount of particle transformation than negative loads.

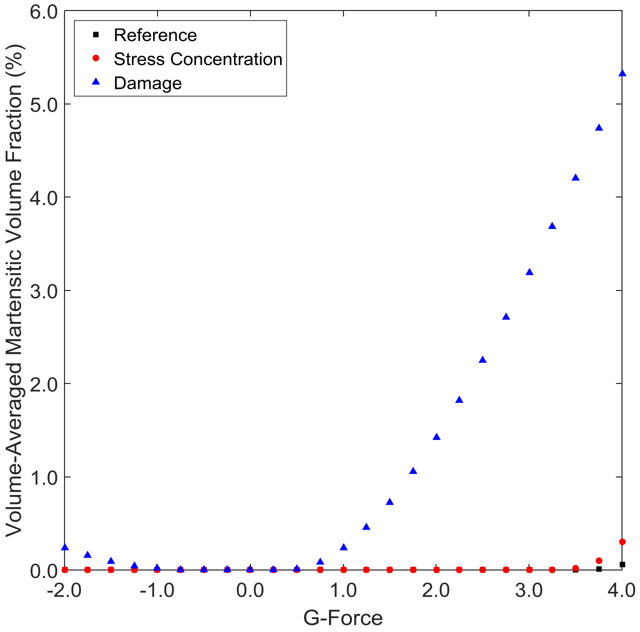

FIGURE 12: Volume-averaged martensitic volume fraction of the particle as a function of wing loading (positive and negative). The particle in the damaged rib experiences a greater amount of transformation due to elevated levels of stress caused by crack propagation. Note also the asymmetric response.

4 CONCLUSIONS

The key results of this paper can be summarized in the following points:

1. A NDE method for detecting fatigue crack formation and propagation has been proposed, exploiting the stress-induced response of sensory particles (particularly SMAs).
2. This method has been computationally demonstrated using a finite element model of a commercial aircraft wing. In particular, substructure modeling was used to reduce the number of variables in the model by nearly 85%. Damage was introduced to this model in the form of a static crack existing in the root rib of the aircraft's wing.
3. While the stress in the undamaged rib induces negligible response from an SMA particle, our studies have shown that a particle in the vacinity of a crack experiences a volume-averaged martensitic transformation of over 5%.

This paper serves to highlight the key aspects of this detection method as well as the advantages that substructure modeling can provide. However, this method can only be truly realized by determining the actual mechanical properties and behavior of SMA particles embedded in a structure. This is currently being addressed in an ongoing attempt to match the experimental behavior of NiTi SMA particles with finite element models. Additionally, there is a need to relate a particle's transformation (MVF) to some detectable response, such as a change in magnetization in MSMAs. Future work will also attempt to determine an optimum location for these particles in a structure as well as explore alternative sensory particle materials and associated sensing methodologies.

5 ACKNOWLEDGMENTS

Finite element analysis was performed using a research license granted by Simulia. Common Research Model finite element files were obtained from NASA.

REFERENCES

[1] Glaessgen, E. H., and Stargel, D., 2012. "The digital twin paradigm for future NASA and US Air Force vehicles". In 53rd Struct. Dyn. Mater. Conf. Special Session: Digital Twin, Honolulu, HI, US, pp. 1–14.

[2] Tuegel, E. J., Ingraffea, A. R., Eason, T. G., and Spottswood, S. M., 2011. "Reengineering aircraft structural

life prediction using a digital twin". *International Journal of Aerospace Engineering,* ***2011***.

[3] Farrar, C. R., and Worden, K., 2007. "An introduction to structural health monitoring". *Philosophical Transactions of the Royal Society A: Mathematical, Physical and Engineering Sciences,* ***365***(1851), pp. 303–315.

[4] Cornell, S. R., Leser, W. P., Hochhalter, J. D., Newman, J. A., and Hartl, D. J., 2014. "Development and characterization of embedded sensory particles using multi-scale 3D digital image correlation". In ASME 2014 Conference on Smart Materials, Adaptive Structures and Intelligent Systems, American Society of Mechanical Engineers, pp. V002T02A010–V002T02A010.

[5] Wallace, T. A., Smith, S. W., Piascik, R. S., Horne, M. R., Messick, P. L., Alexa, J. A., Glaessgen, E. H., and Hailer, B. T., 2010. Strain-detecting composite materials, January. US Patent App. 12/685,280.

[6] Leser, W. P., 2014. "Embedded shape memory alloy particles for the self-sensing of fatigue crack growth in an aluminum alloy.".

[7] Patoor, E., Lagoudas, D. C., Entchev, P. B., Brinson, L. C., and Gao, X., 2006. "Shape memory alloys, part i: General properties and modeling of single crystals". *Mechanics of materials,* ***38***(5), pp. 391–429.

[8] Oishi, R., and Nagai, H., 2005. "Strain sensors of shape memory alloys using acoustic emissions". *Sensors and Actuators A: Physical,* ***122***(1), pp. 39–44.

[9] Karaca, H., Karaman, I., Basaran, B., Chumlyakov, Y., and Maier, H., 2006. "Magnetic field and stress induced martensite reorientation in NiMnGa ferromagnetic shape memory alloy single crystals". *Acta Materialia,* ***54***(1), pp. 233–245.

[10] Version, A., 2013. "6.13". *Analysis Users Guide, Dassault Systems*.

[11] Wu, S.-C., and Haug, E. J., 1988. "Geometric non-linear substructuring for dynamics of flexible mechanical systems". *International Journal for Numerical Methods in Engineering,* ***26***(10), pp. 2211–2226.

[12] Dougherty, J., Padovan, J., and Srivatsan, T., 1997. "Fatigue crack propagation and closure behavior of modified 1070 steel: finite element study". *Engineering Fracture Mechanics,* ***56***(2), pp. 189–212.

[13] Sumi, Y., 1998. "Fatigue crack propagation and computational remaining life assessment of ship structures". *Journal of marine science and technology,* ***3***(2), pp. 102–112.

[14] He, W., Liu, J., and Xie, D., 2014. "Numerical study on fatigue crack growth at a web-stiffener of ship structural details by an objected-oriented approach in conjunction with ABAQUS". *Marine Structures,* ***35***, pp. 45–69.

[15] Rivers, M. B., and Dittberner, A., 2014. "Experimental investigations of the NASA common research model". *Journal of Aircraft,* ***51***(4), pp. 1183–1193.

[16] Kenway, G. K., Martins, J. R., and Kennedy, G. J., 2014. "Aerostructural optimization of the common research model configuration". *Group (ADODG),* ***6***(7), pp. 8–9.

[17] Broeren, A. P., Potapczuk, M. G., Riley, J. T., Villedieu, P., Moëns, F., and Bragg, M. B., 2013. "Swept-wing ice accretion characterization and aerodynamics". *AIAA Paper,* ***2824***, p. 2013.

[18] Vassberg, J. C., DeHaan, M. A., Rivers, S. M., and Wahls, R. A., 2008. "Development of a common research model for applied CFD validation studies". *AIAA paper,* ***6919***, p. 2008.

[19] Lagoudas, D., Hartl, D., Chemisky, Y., Machado, L., and Popov, P., 2012. "Constitutive model for the numerical analysis of phase transformation in polycrystalline shape memory alloys". *International Journal of Plasticity,* ***32***, pp. 155–183.

[20] Hartl, D. J., Chatzigeorgiou, G., and Lagoudas, D. C., 2010. "Three-dimensional modeling and numerical analysis of rate-dependent irrecoverable deformation in shape memory alloys". *International Journal of Plasticity,* ***26***(10), pp. 1485–1507.

[21] NASA, 2014. Common Research Model (CRM) wingbox finite element models. On the WWW, March. URL `http://commonresearchmodel.larc.nasa.gov`.